Optical absorption spectroscopy of reactive oxygen and nitrogen species in a surface dielectric barrier discharge

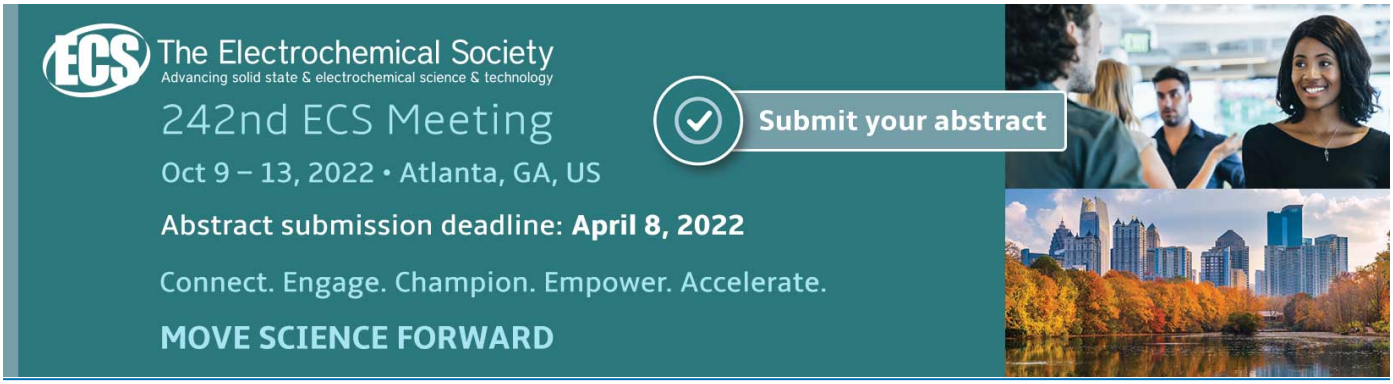

OPEN ACCESS
IOP Publishing
Journal of Physics D: Applied Physics
J. Phys. D: Appl. Phys. **55** (2022) 215205 (15pp)
https://doi.org/10.1088/1361-6463/ac5661

Optical absorption spectroscopy of reactive oxygen and nitrogen species in a surface dielectric barrier discharge

Lars Schücke[1,*], Arisa Bodnar[1], Niklas Friedrichs[1], Alexander Böddecker[1], Niklas Peters[2], Kevin Ollegott[2], Christian Oberste-Beulmann[2], Philipp Wirth[1], Ryan T Nguyen-Smith[1], Ihor Korolov[1], Andrew R Gibson[1,3], Martin Muhler[2] and Peter Awakowicz[1]

[1] Institute of Electrical Engineering and Plasma Technology, Faculty of Electrical Engineering and Information Sciences, Ruhr University Bochum, Bochum, Germany
[2] Laboratory of Industrial Chemistry, Faculty of Chemistry and Biochemistry, Ruhr University Bochum, Bochum, Germany
[3] Research Group for Biomedical Plasma Technology, Faculty of Electrical Engineering and Information Sciences, Ruhr University Bochum, Bochum, Germany

E-mail: schuecke@aept.rub.de

Received 7 October 2021, revised 28 January 2022
Accepted for publication 17 February 2022
Published 28 February 2022

Abstract

A twin surface dielectric barrier discharge (SDBD) ignited in a dry synthetic air gas stream is studied regarding the formation of reactive oxygen and nitrogen species (RONS) and their impact on the conversion of admixed n-butane. The discharge is driven by a damped sinusoidal voltage waveform at peak-to-peak amplitudes of 8 kV_{pp}–13 kV_{pp} and pulse repetition frequencies of 250 Hz–4000 Hz. Absolute densities of O_3, NO_2, NO_3, as well as estimates of the sum of the densities of N_2O_4 and N_2O_5 are determined temporally resolved by means of optical absorption spectroscopy using a laser driven broadband light source, suitable interference filters, and a photodiode detector. The measured densities are acquired across the center of the reactor chamber as well as at the outlet of the chamber. The temporal and spatial evolution of the species' densities is correlated to the conversion of n-butane at concentrations of 50 ppm and 400 ppm, measured by means of flame ionization detectors. The n-butane is admixed either before or after the reactor chamber, in order to separate the impact of short- and long-lived reactive species on the conversion process. It is found that, despite the stationary conversion at the selected operating points, at higher voltages and repetition frequencies the densities of the measured species are not in steady state. Based on the produced results it is presumed that the presence of n-butane modifies the formation and consumption pathways of O_3. At the same time, there is no significant impact on the formation of dinitrogen oxides (N_2O_4 and N_2O_5). Furthermore, a comparatively high conversion of n-butane, when admixed at the outlet of the reactor chamber is observed. These findings are discussed together with known rate coefficients for the reactions of n-butane with selected RONS.

* Author to whom any correspondence should be addressed.

Keywords: dielectric barrier discharge, volatile organic compounds, optical absorption spectroscopy, ozone, reactive oxygen and nitrogen species, nitrogen metastables

(Some figures may appear in colour only in the online journal)

1. Introduction

Non-thermal atmospheric pressure plasmas, such as dielectric barrier discharges (DBDs), are a promising alternative to conventional techniques in the field of purification of industrial exhaust gases or ambient air. Both can be polluted with a wide array of volatile organic compounds, which are known for their negative impact on environment and human health [1–6]. Especially with regard to the removal of volatile organic compounds (VOCs) in air, established processes have a high energy demand and are comparably inflexible in their way of use [7, 8]. Dielectric barrier discharges, however, are potentially more energy efficient and more easily adaptable to a variety of small and large scale applications [9].

Dielectric barrier discharges are characterized by the prevention of an electric arc due to a dielectric material separating the two high voltage electrodes. The resulting properties, such as the non-thermal nature, immediate efficacy, and enhanced formation of reactive species make these discharges suitable for the purification of polluted gas and water feeds, as well as surface treatment [10–12]. Generally, DBDs can be categorized into two basic configurations: the volume dielectric barrier discharge (VDBD) and the surface dielectric barrier discharge (SDBD) [13–15]. In volume DBDs the two electrodes are separated by a gas filled gap, in which the plasma is ultimately ignited. In the case of surface DBDs, however, said gap is completely filled by the dielectric material, resulting in a discharge on its exposed surface [16, 17]. The advantages of SDBDs, especially in the field of air purification, lie in the low flow resistance and ease of optical access for diagnostic purposes, making them ideal for the purification of gas streams, as demonstrated for the removal of VOCs from air. In addition, SDBDs have been shown to generate complex gas flow patterns that transport reactive species throughout the volume, which may also contribute to their success in such applications. [9, 18, 19]

While the efficacy of non-thermal plasmas for the conversion of VOCs has been demonstrated many times, the true reaction kinetics for the oxidation of VOCs by SDBDs remain unclear. Optical absorption spectroscopy (OAS) is a technique employed to gain detailed insight into the gas phase chemistry of a process, by revealing absolute densities of selected reactive species [20–26]. In this work, to gain further understanding on the complex plasma chemistry of the presented process, absolute densities of O_3, NO_2, NO_3, and dinitrogen oxides (N_2O_4 and N_2O_5) are measured temporally and spatially resolved for different n-butane concentrations, which acts as a model VOC [27, 28]. Furthermore, in order to differentiate between the influence of short- and long-lived species, the densities are measured *in situ* and at the reactor outlet while the n-butane is admixed either before the reactor chamber or directly at the outlet. Finally, while considering rate coefficients for selected reactions of n-butane with reactive oxygen and nitrogen species (RONS), it is discussed in how far O_3 and excited nitrogen states may play into the conversion process.

2. Experimental setup

2.1. Surface dielectric barrier discharge

The electrode configuration used to ignite the studied SDBD has been described in detail by Schücke *et al* and Peters *et al* [27, 28]. It is composed of two identical nickel-plated metal grids, symmetrically printed onto front and back side of a thin aluminum oxide plate (α-Al_2O_3). This aluminum oxide plate functions as the dielectric of the SDBD, with the two metal grids acting as driven and grounded electrode. The outer dimensions of the dielectric are $190 \times 88 \times 0.635$ mm and the metallic grid has a lattice constant of 10 mm with the individual traces being 0.45 mm wide. When a high voltage in the order of several kilovolts is applied, the discharge ignites to the sides of the metallic grids, directly on the top and bottom surfaces of the dielectric, as illustrated in figure 1. In dry synthetic air the visible part of the discharge occupies a height of about 0.1 mm measured from the surface of the dielectric with a width of up to 1 mm extending from the sides of the metallic grid [9].

In this work the discharge is driven by a high voltage generator with external transformer (Redline G2000, Redline Technologies, Germany). The generator applies a rectangular high voltage pulse at repetition frequencies between 250 Hz and 4 kHz to the primary side of the transformer. On the secondary side the transformer's inductance and the electrode's capacitance form a resonant circuit, resulting in a high voltage damped sine wave with an eigenfrequency of 86 kHz and amplitudes of up to 13 kV_{pp}, which then drives the discharge. The dissipated powers of the system are in the range of 0.5 W at 250 Hz and 8 kV up to 70 W at 4 kHz and 11 kHz. Reproducible values for all operating points under the same conditions have been measured before and can be found in [27]. A gas flow of 10 slm of synthetic air (ALPHAGAZ 1 Luft, AIR LIQUIDE Deutschland GmbH, Germany) is provided by means of mass flow controllers (EL-FLOW Select, Bronkhorst High-Tech B.V., Netherlands) for all measurements in this work. This results in a spatially averaged gas stream velocity of 0.1 ms^{-1} at a constant pressure of 1 bar.

2.2. Reactor chamber and devices

The experimental setup (see figure 2) and methodology used for all measurements in this work is similar to the one presented by Schücke *et al* [27], with the exception of a few

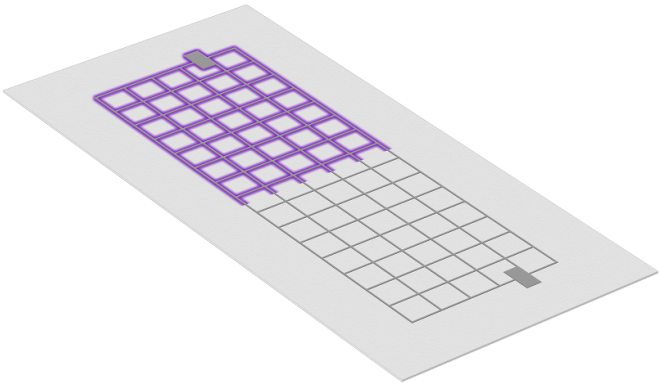

Figure 1. Sketch of the electrode configuration used to ignite the SDBD. The plasma ignites on both sides of the system, directly next to the driven (top) and grounded (bottom) metallic grid. For illustrative purposes the image is split into two parts, with (top half) and without (bottom half) an active plasma. [27] © Institute of Physics (the 'Institute') and IOP Publishing Limited 2019. n/a.

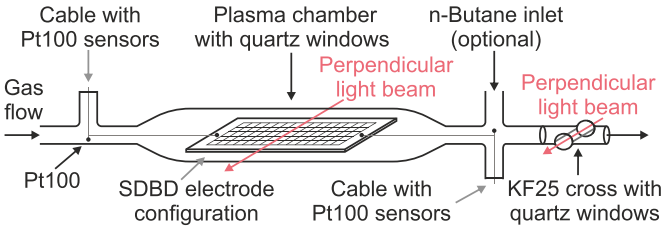

Figure 2. Schematic drawing of the reactor chamber and periphery. Optical absorption measurements are performed either across the electrode configuration or through the KF25 cross attached to the chamber outlet. The power connectors are not shown for the sake of simplicity.

modifications. The aluminum vessel that serves as the reactor chamber and ensures a defined synthetic air atmosphere has been modified to accommodate for larger, rectangular quartz windows (Viosil SQ, GVB GmbH, Germany). Two such windows with dimensions of 75 × 15 mm are located to either side of the discharge to provide optical access perpendicular to the gas flow. These windows have been used for all optical absorption measurements shown in sections 4.1 and 4.2. The transmission of the used quartz, as measured by the manufacturer, is over 90% in the range from 200 nm to 1900 nm.

Four Pt100 resistance thermometers, which measure the upstream and downstream gas and electrode temperatures, were added using vacuum feed-throughs in the KF25 tubing (Pfeiffer Vacuum Components & Solutions GmbH, Germany) before and after the chamber. The sensors are connected to the LabVIEW user interface (LabVIEW 2019, National Instruments Corporation, USA) by means of a PLC control system (KL3204, Beckhoff Automation GmbH & Co. KG, Germany). The downstream tubing also serves as an additional, optional inlet for VOCs, to separate the influence of plasma and longer-lived reactive species on the conversion process. A further KF25 cross with quartz windows (Pfeiffer Vacuum Components & Solutions GmbH, Germany) allows for optical access of the exhaust gas stream directly after the reactor chamber. Finally, the chamber was mounted on a motorized stage (LTS150, Thorlabs Inc. USA), to allow for measurements axially resolved along the length of the electrode (see chapter 4.2).

3. Diagnostic methods

3.1. Flame ionization detectors

Two flame ionization detectors (SmartFID ST, ErsaTec GmbH, Germany) are used to measure absolute concentrations of the admixed organic compounds, in this study n-butane (2N5, AIR LIQUIDE Deutschland GmbH, Germany) specifically. The operating principle and measurement procedure were presented in detail by Schücke *et al* [27]. In summary, the two devices are directly connected to the setup before and after the reactor chamber, drawing a continuous sample of the gas stream and providing real time data on the VOC's concentrations and, by automated calculations, the absolute and relative conversion. These values are crucial for the understanding of the processes underlying chemistry and complemented by measurements of RONS, as outlined in the following section.

3.2. Optical absorption spectroscopy

Optical absorption spectroscopy is a technique that correlates the absorbance of light transmitted through a medium with given properties based on the Lambert-Beer law, according to equation (1).

$$I_1 = I_0 \cdot \exp(-\sigma(\lambda, T) \cdot n \cdot l). \tag{1}$$

The medium is characterized by its density n, its effective absorption cross section $\sigma(\lambda, T)$ (where λ is the wavelength and T the temperature) and the absorption length l, which corresponds to the width of the reactor. Due to absorption within the medium, the initial light intensity I_0 is reduced to a lower value I_1 after transmittance. The light emitted by the plasma and ambient lighting would normally have to be subtracted from these values, but can be neglected in the presented case. Here, the light emitted from the very thin plasma does not reach the detector and the ambient light was sufficiently dimmed. The Lambert-Beer law can then be solved for the medium's density, which can be calculated as shown in equation (2).

$$n = \frac{-\ln\left(\frac{I_1}{I_0}\right)}{\sigma(\lambda, T) \cdot l}. \tag{2}$$

The absolute densities of reactive oxygen and nitrogen species presented in this work are acquired using a setup for OAS as shown in figure 3. The divergent light of a thermally stabilized (TECMount 284, Arroyo Instruments LLC, United States) laser-driven xenon discharge broadband lamp (EQ-99X LDLS, Energetiq Technology Inc. United States) is focused into a parallel beam by a plano-convex quartz collimating lens (#48-274, Edmund Optics Ltd United Kingdom) and restricted by an iris diaphragm in order to avoid

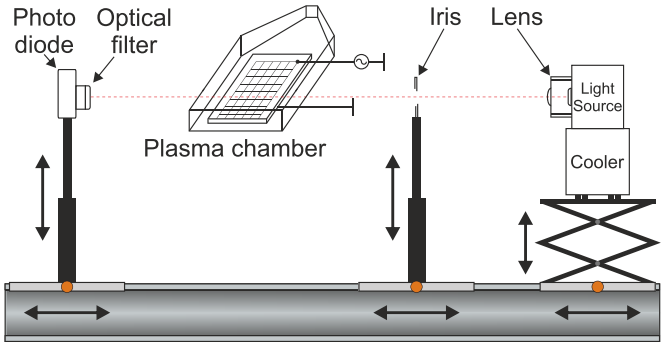

Figure 3. Schematic drawing of the optical absorption spectroscopy setup.

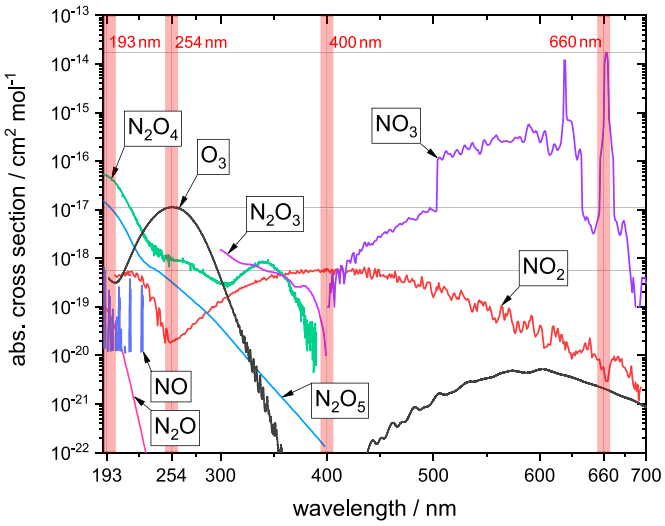

Figure 4. Absorption cross sections of the considered reactive oxygen and nitrogen species [29]. Wavelength sections accepted by the bandpass filters (see table 1) are highlighted in red.

distortions at the lenses edges and restrict possible reflections. The light beam then passes through the reactor chamber, perpendicular to the gas flow, and falls onto a photodiode (APD440A2, Thorlabs Inc. United States). The front of the photodiode is equipped with an interference filter suitable for the desired wavelength, based on the absorption cross section of each species $\sigma(\lambda)$ according to figure 4. With the exception of NO_3 the absorption cross-sections of the measured species are approximately constant across transmission region of each bandpass filter. In the case of NO_3 this would mean that a deconvolution and integration of the transmission function of the bandpass filter and the profile of the NO_3 absorption cross-section is required. However, as no significant absorption related to NO_3 could be detected under our operating conditions it was not necessary to implement this correction.

All absorption measurements are performed continuously in time while the experimental parameters are varied, with pauses of 90 s before and after changing each voltage setting. The entire parameter variation procedure is the same as that described in detail in Schücke *et al* [27]. The initial light intensity I_0 is checked before and after each measurement series, when the plasma is turned off and the gas in the chamber has been exchanged (see figure 5), in order to ensure there is no drift of the value. A typical value for the intensity drift of the lamp over one measurement period (15 min), as recorded by the photodiode, is 0.6%.

The individual wavelengths at which the absorption spectroscopy is performed for each reactive species were chosen based on two criteria: the respective absorption cross section being as high as possible while also being sufficiently higher than any other cross section in that wavelength area. The bandpass filters (Edmund Optics Ltd United Kingdom) chosen according to these criteria are listed in table 1. It should be noted that for N_2O_4 and N_2O_5 the difference in absorption cross section at 193 nm is about 72%, which means there is no sufficient distinction between these two species. As a compromise their densities are measured as the sum of both species while using the higher absorption cross section of N_2O_4 for the Lambert-Beer law. It should be noted that if the cross section for N_2O_5 was chosen for the calculation, the resulting density would differ significantly. As a result of these factors, the densities presented for these species in this work represent an estimate of the 'effective density' of N_2O_4 and N_2O_5, rather than a density that can conclusively be related to one species or the other. Due to its comparatively high density, as measured at 254 nm, the absorption caused by O_3 at 193 nm needs to be subtracted from these numbers to achieve are more accurate representation of the densities of N_2O_4 and N_2O_5. An estimate of this effect can be obtained using equation (3), where $n_{193\ \mathrm{nm}}$ is the effective total density of reactive species measured at 193 nm using the absorption cross-section of N_2O_4 and $n_{O_3,254\ \mathrm{nm}}$ is the density of ozone measured at 254 nm. The latter is then weighted by the ratio of the absorption cross-sections of O_3 and N_2O_4 at 193 nm, $\sigma_{O_3,193\ \mathrm{nm}}$ and $\sigma_{N_2O_4,193\ \mathrm{nm}}$ as given by figure 4.

$$n_{N_2O_4,N_2O_5} = n_{193\ \mathrm{nm}} - n_{O_3,254\ \mathrm{nm}} \cdot \frac{\sigma_{O_3,193\ \mathrm{nm}}}{\sigma_{N_2O_4,193\ \mathrm{nm}}}. \quad (3)$$

The absorption spectroscopy procedure as described above has been checked for viability for each bandpass region. For all regions the absorption by the VOCs' reaction products should be negligible, due to their low concentrations [27]. Furthermore, the blocking regions of all filters extend across the full sensitivity range of the used photodiode detector (200 nm to 1000 nm), which rules out possible influences of other species in secondary bandpass regions of the filters. The intensity of the measured signal is adjustable by the amplification of the photodiode. Neutral density filters are used to ensure the linearity of the signal and avoid saturation for each filter and amplification setting. This is especially important for the UV range, as UV light may be absorbed by the used quartz glass windows and atmospheric oxygen. The manufacturer reports a transmission for the quartz windows of over 90% across the sensitivity range of the photodiode. Even at 193 nm no significant decrease of the voltage signal from the photodiode is observed. Further absorption of UV light due to atmospheric oxygen, specifically at 193 nm, can be calculated according to the Lambert-Beer law and the corresponding

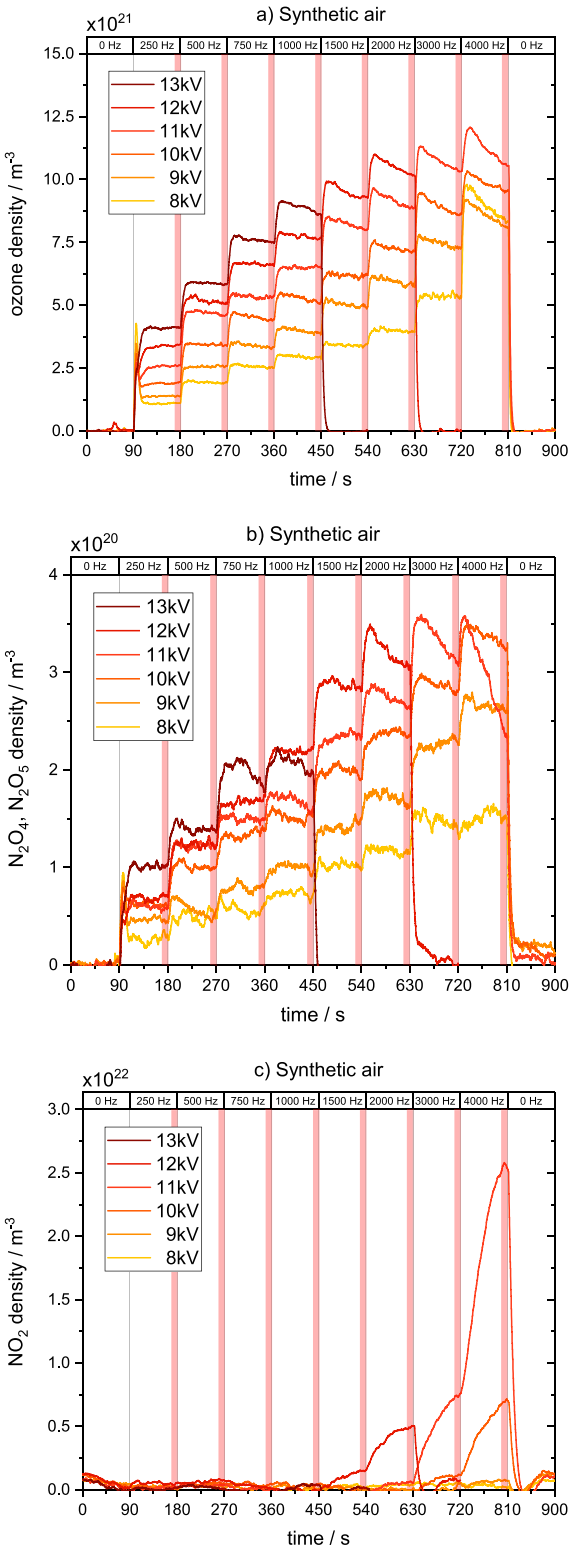

Figure 5. Time-resolved densities of O_3, effective N_2O_4 and N_2O_5, as well as NO_2, measured across the center of the discharge without the admixture of n-butane. Red highlights indicate the 10 s intervals where the values were averaged for each voltage and frequency setting for the following graphs.

absorption cross-section ($3.9 \cdot 10^{-27}\,m^2$ [29]). The amount of light absorbed in this way amounts to 1.8% of the initial intensity emitted by the light source.

Table 1. List of measured species with the respectively used filters' center wavelength and full width at half maximum, as well as the suppliers item number.

Species	Filter range / nm	EO item number
N_2O_4, N_2O_5	193.0 ± 7.5	#67-836
O_3	254.0 ± 5.0	#67-808
NO_2	400.0 ± 5.0	#65-677
NO_3	660.0 ± 5.0	#11-981

The photodiode has a circular active area of 1 mm diameter which faces the reactor chamber side window and is positioned in the center of the light spot projected by the light source. The absorption length l is given by the reactor width of 10 cm. The aforementioned motorized stage, which allows translation of the chamber in direction of the gas stream, is not shown for the sake of simplicity.

The spatial resolution for all measurements is in the order of 1 mm, as given by the active area of the photodiode, illuminated be the approximately parallel light beam formed by light source and lenses.

4. Results and discussion

4.1. Temporal evolution of the densities

Absolute densities of reactive oxygen and nitrogen species in combination with varied concentrations of VOCs and their conversion performance are crucial to further understand the underlying chemistry of the process. In this study O_3, NO_2, NO_3, and a combination of N_2O_4 and N_2O_5 were measured spatially averaged across the middle of the electrode configuration, separately above and below the electrode, along the electrode configuration in the direction of the gas flow, and in the exhaust after the reactor chamber. For all shown graphs, except figure 5, at least three full sets of measurements have been performed and error bars are given by the standard deviation of these measurements. The highest absolute error experienced across each individual graph is applied to each data point within that graph in place of a systematic error.

The underlying chemistry of the process, based on atomic oxygen, atomic nitrogen, ozone, and nitrogen oxides is relatively complex and has a delicate, temperature dependent balance. Computational models of this chemistry in surface DBDs have been presented in a number of studies in the literature [30, 31]. In these studies, the formation of NO-based species is proposed to be initiated by the interaction between vibrationally excited nitrogen molecules and O, to form NO and N. The resulting NO is then involved in the formation of NO_2 by reacting with O or O_3. Reactions involving NO_2 then go on to produce N_2O, NO_3, N_2O_3, N_2O_4, and N_2O_5. Overall, the kinetics and densities of these species are closely coupled. For processes in closed chambers, without a gas flow, Park *et al* have identified a number of specific reactions of importance based on production rates [31]. These include the formation of N_2O_4 and N_2O_5 from NO_2 and NO_3, as well as the formation of NO_2 from O_3 and NO. The formation of NO_2

from O and NO, as well as its destruction involving O do not appear to play a significant role. While these studies provide some insight into the reactions that may be important in our system, the detailed impact on the following measurements is difficult to discern, due to differences in the experimental systems, in particular, the presence of a gas flow that continuously refreshes the gas within the plasma region.

Figure 5 shows the time resolved behaviour of the measured species across the center of the discharge and for dry synthetic air without the admixture of n-butane. Especially for higher voltages and frequencies no steady state of the densities of the reactive species is achieved during the 90 s time interval, which was chosen for comparability with the results in Schücke *et al* [27]. Nevertheless, in the same work, it was shown that the VOC conversion does achieve steady state within 90 s, which is in contrast to the non-stationary state of the measured species and suggests a low correlation between the densities of these reactive species and VOC conversion. The three graphs also illustrate how the measurement values have been condensed into graphs with density over repetition frequency. For each combination of voltage and frequency the last 10 s, highlighted in red, are averaged and reduced to a single data point of the following graphs in this work.

The O_3 densities, shown in figure 5(a), first increase with higher voltages and repetition frequencies, i.e. with higher dissipated power, and then show a decline within the measurement interval for higher powers. This is most likely a result of increasing temperatures as the plasma is operated for long time periods, which affects the rate constants for production and consumption of O_3. To complement this observation, the temporally resolved temperatures of the upstream and downstream ends of the dielectric plate, as well as the exhaust gas stream are presented in appendix figure A1. As these measurements show, a steady state of the different temperatures is generally not achieved and, by extrapolation, it would take up to 60 min per parameter combination to do so. However, as previous measurements have shown (see Schücke *et al* [27]), the VOCs' conversion achieves steady state after less than 90 s. Furthermore, in the range from 300 to 350 K the absorption cross section of O_3 decreases by 3.4% [32]. As the standard deviation of these measurements is consistently higher than that, the temperature dependency of the absorption cross section, as well as the non steady state of the temperatures, is neglected.

The effective density of N_2O_4 and N_2O_5 in figure 5(b) exhibits a similar qualitative behaviour to that of O_3. In stark contrast to that is the density of NO_2, shown in figure 5(c), which is challenging to measure with the same setup due to a comparatively low absorption cross section. It can be seen that for lower power settings the NO_2 density is below the measurement threshold, yet drastically increases at higher power settings between 10 W and 70 W. These operating points coincide with those where the densities of O_3 and effective N_2O_4/N_2O_5 show a stronger decline, hinting at an overall change in the importance of different reaction pathways for these species. Finally, despite the comparably high absorption cross section, no absorption could be detected due to NO_3 using the presented setup.

4.2. Spatial distribution of reactive species

The electrode geometry of the SDBD used in this study is ultimately intended for industrial application and not optimized for ease of diagnostic accessibility, which makes the system quite complex. In order to complement the time resolved density measurements and the illustration of the measurement procedure, spatially resolved densities of O_3 and the combination of N_2O_4 and N_2O_5 were measured for a representative medium power setting of 11 kV_{pp} and 1 kHz above and below the dielectric plate and along the flow direction of the gas stream. For both measurements the beam from the light source, with a diameter of approximately 1 mm, was guided through the center of the visible region between the dielectric plate and the reactor wall. The results of these measurements are presented in figure 6, where the midpoint of the electrodes is in the center of the horizontal axis (at 31 mm). It is clear that the densities of the reactive species above the electrode configuration are consistently higher than those below. Furthermore, a periodic variation of densities can be observed. This variation coincides with the positioning of the electrode grid lines perpendicular to the gas stream, which are indicated by grey vertical lines. Both effects are expected to be caused by the flow characteristics of the gas stream, disturbed by the plasma and thermal effects (e.g. thermal expansion and buoyancy), which was studied by means of Schlieren imaging by Offerhaus [9]. The Schlieren images presented in Offerhaus' work clearly show periodic disturbances of the gas stream coinciding with the perpendicular grid lines, as well as differences in the disturbances above and below the electrode configuration. This also suggests, in addition to local variations of the total gas stream density, possible changes in the local gas phase chemistry and densities of reactive species.

4.3. Densities of reactive species for varying n-butane content in the plasma chamber

The dependence of the densities of the reactive species on the amount of admixed VOC and its conversion may lead to further insight into the complex reaction mechanism that enables the oxidation. Figure 7 shows the O_3 densities across the center of the system, and for n-butane concentrations of 0 ppm, 50 ppm, and 400 ppm exemplarily at 11 kV_{pp}. The full set of measurements can be found in appendix figure A2.

At lower pulse frequencies and voltages, i.e. lower dissipated powers, an increase of the O_3 density towards higher powers can be observed. For even higher voltages and pulse frequencies the O_3 densities begin to decrease again. As illustrated in chapter 4.1 the decline of the O_3 densities for higher dissipated powers may be caused by increased temperatures of the dielectric plate and the gas stream. It is yet unclear in how far the formation of other species may instead inhibit the formation of O_3, or cause a decay via different reaction pathways, and lead to decreased O_3 densities at certain operating conditions due to such effects. Nevertheless, it should also be noted that the rate coefficient for the decomposition of O_3 into the more reactive atomic oxygen is temperature

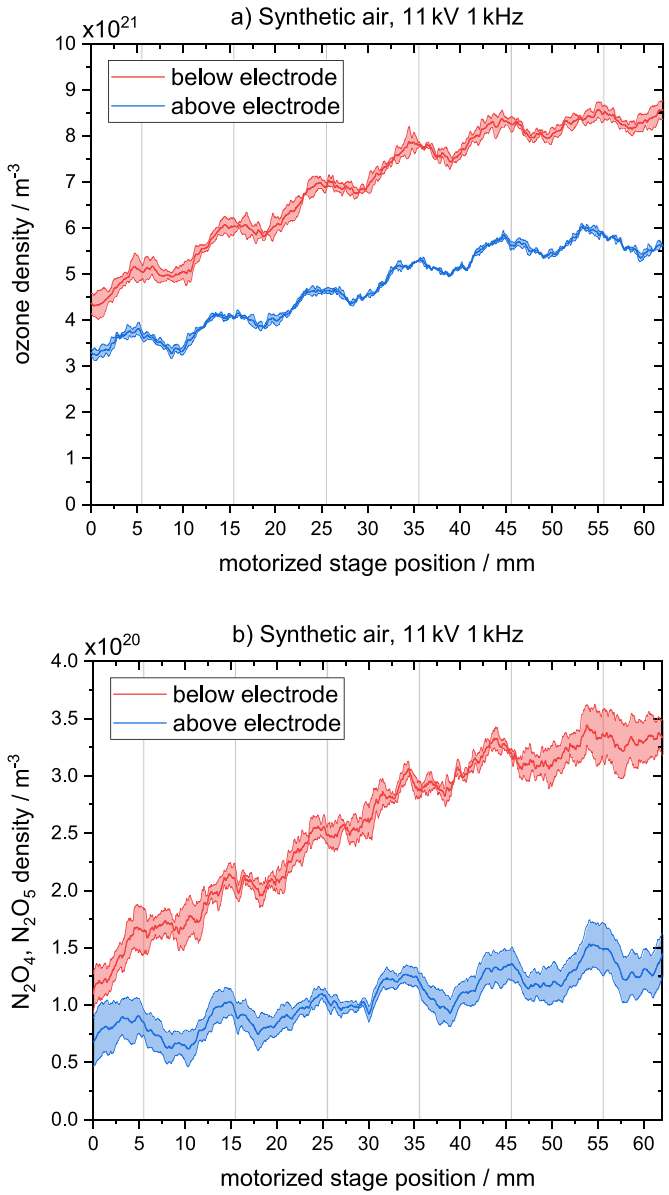

Figure 6. Densities of (a) O_3 as well as (b) effective N_2O_4 and N_2O_5 along the length of the electrode configuration without the admixture of n-butane. Grey vertical lines indicate the positions of the electrode grid lines perpendicular to the gas flow. The center of the *x*-axis corresponds to the center position along the reactor.

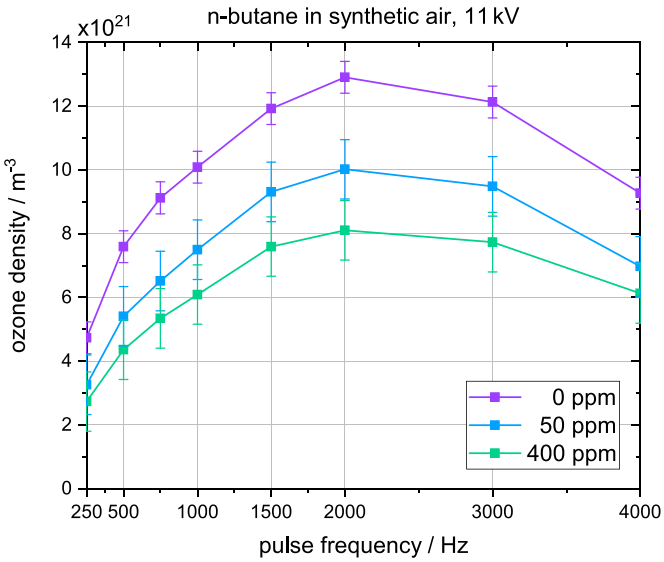

Figure 7. Densities of ozone measured across the center of the discharge at 11 kV_{pp} for 0 ppm, 50 ppm, and 400 ppm of n-butane admixed before the reactor chamber.

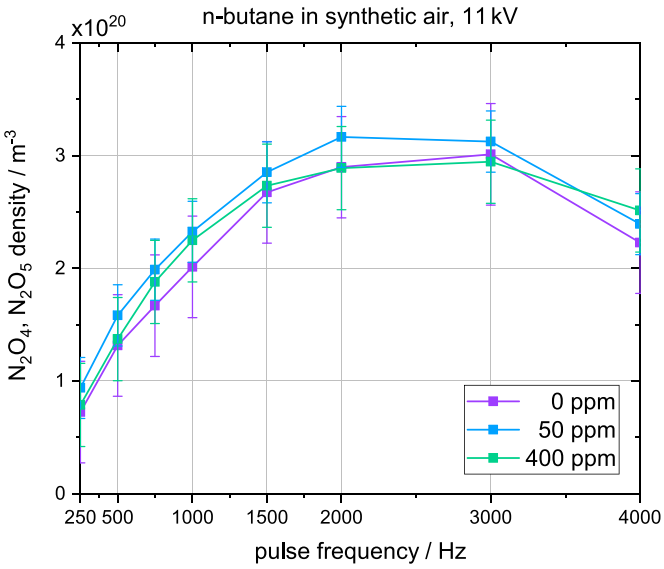

Figure 8. Effective densities of N_2O_4 and N_2O_5 measured across the center of the discharge at 11 kV_{pp} for 0 ppm, 50 ppm, and 400 ppm of n-butane admixed before the reactor chamber.

dependent [33]. A sufficient gas temperature of around 100 °C, for this mechanism to be of relevant magnitude, is not reached under the presented operating conditions, as will be illustrated in greater detail in section 4.4.

Furthermore, it can be observed that the addition of larger amounts of n-butane leads to a stronger decrease of the O_3 densities, which cannot be observed in the case of N_2O_4 and N_2O_5 as presented in figure 8 (full set of measurements in appendix figure A3). This would hint at a direct interaction between O_3 and n-butane, or even a direct oxidation of the latter. However, it is also possible that, due to the presence of n-butane, the reaction pathways leading to the formation of O_3 change. This might be due to interaction of, e.g. atomic oxygen, which is required to form O_3, and the admixed n-butane, such that less atomic oxygen is available for the formation of O_3. At the same time the reaction pathways leading to the formation of N_2O_4 and N_2O_5 appear to be largely unaffected. This hypothesis will be further explored in the following section, where n-butane has been admixed after the plasma chamber as well, while also considering the conversion of n-butane depending on the location of admixture.

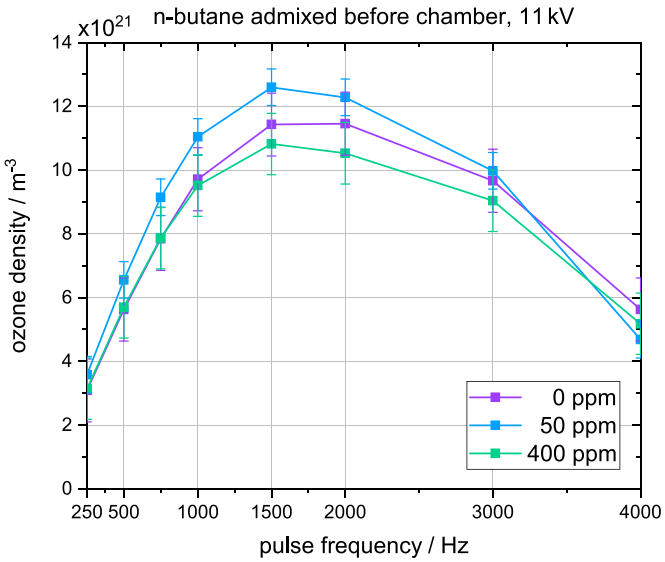

Figure 9. Densities of O_3 measured at 11 kV_{pp} in the exhaust for 0 ppm, 50 ppm, and 400 ppm of n-butane admixed before the plasma chamber.

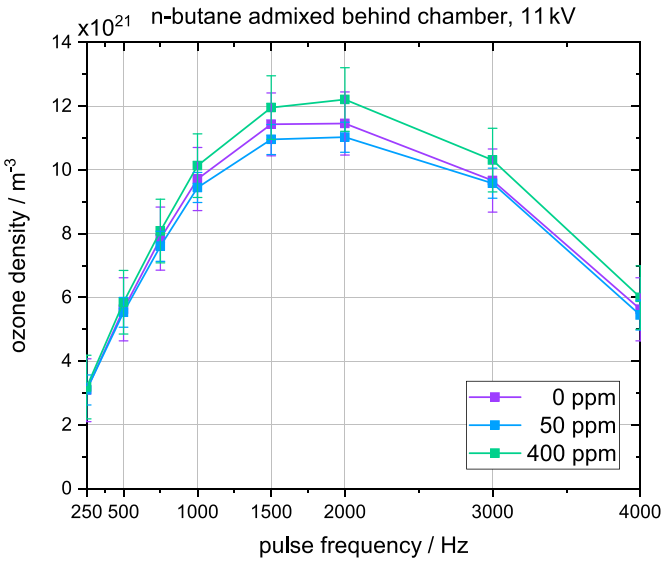

Figure 10. Densities of O_3 measured at 11 kV_{pp} in the exhaust for 0 ppm, 50 ppm, and 400 ppm of n-butane admixed behind the plasma chamber.

4.4. Densities of reactive species for varying n-butane content in the exhaust gas stream

In order to further elucidate the importance of reactive species with different lifetimes, O_3 densities have also been measured after the reactor chamber, rather than within the reactor chamber (see figure 2). The densities of O_3 at this position in the exhaust are shown in figure 9, for pure synthetic air and for butane admixed, as before, in front of the reactor chamber (full set of measurements in A figure A4). Short-lived reactive species are present only in the region close to the plasma. To exclude the influence of such species on the conversion of n-butane, O_3 densities were also measured for butane admixed after the reactor chamber but still in front of the measurement position of the densities of the reactive species (figure 10, full set of measurements in appendix figure A5). In both cases the start of the decrease of absolute densities occurs sooner (i.e. at lower voltages and pulse frequencies) than when measured within the reactor. This is possibly caused by more elevated temperatures of the gas stream, having passed the full length of the discharge, as when measured across the center of the reactor.

For the measurements with n-butane admixed before the reactor chamber, unlike in figure 7, there is no longer a significant difference between the O_3 densities at 0 ppm, 50 ppm, and 400 ppm of n-butane. This indicates that the presence of n-butane in the mixture affects the production rate of O_3 as a function of distance along the reactor and the distance required to achieve an equilibrium density, but not the equilibrium value itself. These findings imply a change of the reaction pathways for the production and/or consumption of O_3. Furthermore, when n-butane is admixed after the reactor chamber, similar densities are observed (see figure 10). This is another indication that O_3 does not directly interact with the VOC, and rather that the formation of O_3 is inhibited in the presence of n-butane, possibly due to oxidation of n-butane by atomic oxygen, which is required for the formation of O_3. To give an indication of the rate at which plasma-produced reactive species are expected to react with n-butane, a number of rate coefficients are given in table 2.

Table 2. Rate coefficients of reactions between n-butane and selected RONS to various products at 298 K as compiled in [45]. (* Rate coefficient given as sum for all listed reactions with different products.).

Reaction	k(298 K) / cm^3s^{-1}	Source
$C_4H_10 + O$	$2.46 \cdot 10^{-14}$	[36]
$C_4H_10 + O_2(^1D)$	$1.74 \cdot 10^{-18}$	[37]
$C_4H_10 + O_3$	$1.00 \cdot 10^{-23}$	[38]
$C_4H_10 + NO_2[^*]$	$1.56 \cdot 10^{-30}$	[34]
$C_4H_10 + NO_3$	$4.65 \cdot 10^{-17}$	[39]
$C_4H_10 + H$	$6.87 \cdot 10^{-16}$	[40]
$C_4H_10 + OH[^*]$	$2.33 \cdot 10^{-12}$	[35]
$C_4H_10 + N(^2D)$	$3.10 \cdot 10^{-11}$	[41, 42]
$C_4H_10 + N(^2P)$	$2.70 \cdot 10^{-12}$	[41, 43]
$C_4H_10 + N_2(A^3\Sigma_u^+)$	$2.70 \cdot 10^{-12}$	[41, 44]

It should be noted that the product distributions for many of these reactions are not known, and therefore it is not yet possible to use these as part of a detailed plasma chemistry model. However, for the reactions of n-butane with NO_2 and with OH some reaction products are known. Possible reaction products for n-butane and NO_2 are 1-C_4H_9, sec–C_4H_9, cis–HONO, and trans–HONO, with the rate coefficients favouring the production of 1-C_4H_9 [34]. The listed reaction products for n-butane and OH are again 1-C_4H_9, sec–C_4H_9, with both reactions also

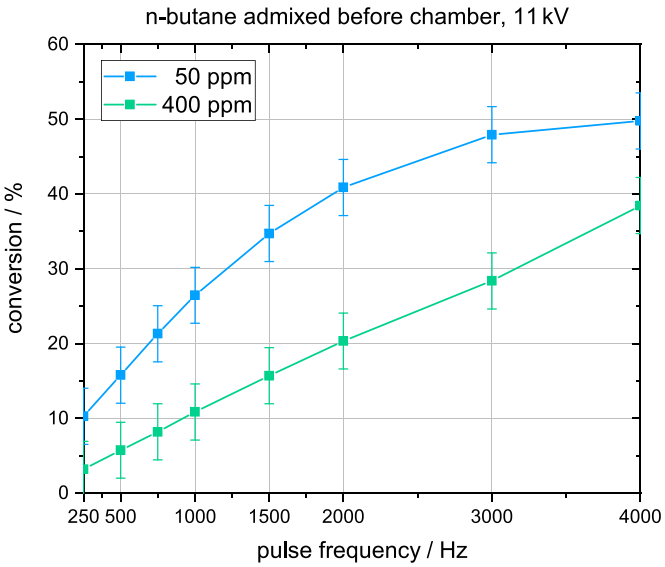

Figure 11. Relative conversion of n-butane admixed before the reactor chamber at 11 kV_{pp} and for concentrations of 50 ppm and 400 ppm.

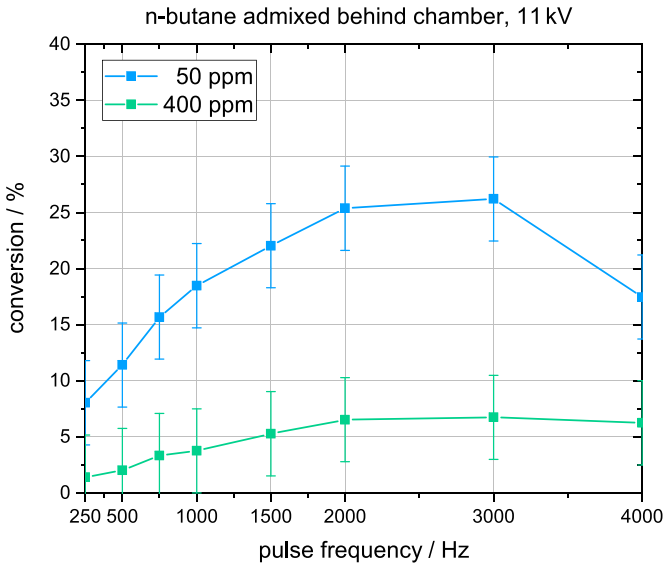

Figure 12. Relative conversion of n-butane admixed after the reactor chamber at 11 kV_{pp} and for concentrations of 50 ppm and 400 ppm.

leading to the formation of H_2O. Here, the rate coefficients indicate that 1-C_4H_9, sec–C_4H_9 are formed in similar amounts [35]. For ease of comparison these rate coefficients have been summed up in table 2, to be used as a general guide to possible reaction pathways. For example, the rate coefficient for the reaction of n-butane with O_3 is nine orders of magnitude lower than that of n-butane with O. This low rate coefficient is consistent with the observations that the O_3 density is not strongly affected by the presence of n-butane in the gas mixture at the concentrations studied here.

The conversion of n-butane has been measured for concentrations of 50 ppm and 400 ppm when admixed before the reactor chamber (figure 11) and after the reactor chamber (figure 12). Full sets of measurements are given in appendix figures A6 and A7. The maximum conversion of n-butane when admixed before the reactor chamber, across the tested parameter set, is 50% at a concentration of 50 ppm and the most intense setting for the plasma of 11 kV_{pp} and 4 kHz. At a higher concentration of 400 ppm the conversion is consistently lower but still significant. When n-butane is admixed after the reactor chamber the conversion reaches a maximum value of 26%. This value is much higher than expected, as the atomic oxygen, present when n-butane is admixed before the reactor chamber, is believed to play a key role for the oxidation process [46]. At a concentration of 400 ppm of n-butane, however, the conversion achieves significantly lower values than when admixed before the reactor chamber. This behaviour may be due to depletion of reactive species outside of the active zone, which would only be within the reactor, or due to the absence of sufficient mixing of the gas stream as induced by the discharge within the reactor (as shown by Offerhaus [9]).

The conversion of n-butane purely based on O_3 can be estimated under a few assumptions. Total oxidation of the molecule and its intermediate products is assumed according to equation (4). Based on the residence time from the n-butane inlet after the chamber to the inlet of the FID (2.2 s) the temporal evolution of each intermediate product's density can be calculated according to equation (5). Since the rate coefficients for each intermediate step are unknown, the one for the initial reaction of n-butane and O_3, according to table 2, is assumed for these reactions. For each step of the oxidation process the change in density of the respective reaction product $\mathrm{d}n_i$ over the time interval $\mathrm{d}t$ is produced by a reaction of the previous step $\mathrm{d}n_{i-1}$ and consumed towards the next step by reaction of $\mathrm{d}n_i$, each multiplied by the ozone density n_{O_3} and the rate coefficient k_{ox,O_3}. As full oxidation is necessary for the FID to not measure any signal of a carbon-containing molecule, a theoretical conversion X_{total} can be estimated according to equation (6), where the sum of the remaining n-butane n_0 and each of its reaction products n_i are divided by the initial density of n-butane n_{init}.

$$\mathrm{C_4H_{10}} + 13\ \mathrm{O_3} \longrightarrow 4\ \mathrm{CO_2} + 5\ \mathrm{H_2O} + 13\ \mathrm{O_2} \tag{4}$$

$$\frac{\mathrm{d}n_i}{\mathrm{d}t} = k_{\mathrm{ox},O_3} \cdot n_{i-1} \cdot n_{O_3} - k_{\mathrm{ox},O_3} \cdot n_i \cdot n_{O_3} \left[\frac{\mathrm{m}^{-3}}{\mathrm{s}}\right] \tag{5}$$

$$X_{\mathrm{total}} = 1 - \frac{n_0 + \sum_{i=1}^{12} n_i}{n_{\mathrm{init}}}. \tag{6}$$

In this case the response factors of the FIDs for each individual intermediate product are unknown and neglected. When calculated for the operating points with the highest O_3 densities measured after the reactor chamber, $1 \cdot 10^{22}\ \mathrm{m}^{-3}$ for 50 ppm of n-butane and $8 \cdot 10^{21}\ \mathrm{m}^{-3}$ for 400 ppm of n-butane, a conversion far below the measurement threshold is obtained.

The calculated values are in the order of $1 \cdot 10^{-13}\%$, which is significantly lower than the measured values. This points to the importance of other long-lived reactive species, in order to enable the conversion of n-butane in the absence of short-lived reactive species. Among the reactions documented in [45] (see table 2) the nitrogen metastable $N_2(A^3\Sigma_u^+)$ is a possible candidate. While collisions with $N_2(A^3\Sigma_u^+)$ cannot directly cause oxidation, the large internal energy of the excited state could cause excitation or fragmentation of the n-butane molecule. These reaction products would have the potential to react at a higher rate with other plasma produced species, such as O_3.

Another effect to be considered is the thermal decay of O_3 into molecular oxygen and atomic oxygen, which is highly temperature-dependent and may facilitate the oxidation of n-butane through atomic oxygen, even after the outlet of the chamber. The rate coefficient for the thermal decomposition has been studied in detail with results being documented in NIST Chemical Kinetics Database according to equation (7), where R is the molar gas constant and T_g is the neutral gas temperature [33].

$$k(T_g) = 7.6 \cdot 10^{12} \exp\left(-\frac{102\,268\,\mathrm{J\,mol^{-1}}}{RT_g}\right) \mathrm{s^{-1}}. \quad (7)$$

Even under the drastic overestimation that the gas temperature is 110 °C (to be in accordance with the defined region of the rate coefficient for the thermal decay of O_3), the total conversion of 50 ppm of n-butane admixed after the reactor chamber based on atomic oxygen formed due to the thermal decomposition of O_3 (and O_3 itself) amounts to $4.25 \cdot 10^{-5}\%$. For a concentration of 400 ppm that number decreases to just $1.1 \cdot 10^{-12}\%$. The addition of other reactive species using their measured densities, due to their significantly lower rate coefficients for the oxidation of n-butane, does not make a notable difference to these results. These findings support the hypothesis that further long-lived species, other than the measured reactive oxygen and nitrogen species, play a significant role in the conversion process, potentially by breaking chemical bonds and enabling direct oxidation from reactive species.

5. Conclusion and future work

A surface dielectric barrier discharge intended for the conversion of volatile organic compounds is studied with regard to gas phase chemistry by optical absorption spectroscopy of reactive oxygen and nitrogen species. Densities are measured within the reactor chamber and in the outlet. To differentiate between the influence of short-lived and long-lived reactive species the VOC (n-butane) is admixed either before or after the chamber. A variation of the driving voltage, pulse frequency, and VOC concentration is performed in order to uncover trends in different operating regimes based on dissipated power and gas temperature.

Temporal evolutions of the densities of O_3, effective N_2O_4 and N_2O_5, as well as NO_2 measured in pure synthetic air show a direct correlation between the densities of reactive species and the dissipated power based on repetition frequency and voltage amplitude. At higher gas temperatures a decay of O_3 and the dinitrogen oxides is observed, while the densities of NO_2 suddenly increase at the corresponding operating points. This indicates a turnaround in the operating regime which does, however, not appear to have a significant influence on the discharge's performance with regard to VOC conversion. Significant amounts of NO_3 are not found for any of the applied operating points.

Further spatially resolved measurements uncover a difference of O_3 and dinitrogen oxide densities above and below the electrode configuration, as well as along the the electrode. The densities below the electrode configuration are consistently higher than above, which is attributed to thermal effects. Along the electrode densities grow substantially with the gas streams continued exposure to the discharge and exhibit oscillations, which coincide with the electrode geometry. This effect could be connected to gradients of the absolute gas density, but also to local differences in the gas phase chemistry, as will be further explored by Schlieren imaging in a different work on the same discharge.

When adding a VOC in form of n-butane an effect on the densities of O_3 within the reactor chamber is observed, with no significant changes in the effective densities of N_2O_4 and N_2O_5. However, in the outlet of the reactor, after having passed the entire length of the discharge, the O_3 densities no longer exhibit a strict dependence on the n-butane admixture. When admixed after the reactor chamber, the presence of n-butane does not have a significant effect on the measured O_3 densities, which, together with the former observations, suggests a change of reaction pathways for the formation of O_3, rather than consumption of it in an oxidative process. This conclusion is further supported by the rate coefficient for the reaction of O_3 with n-butane, which is comparatively low (see table 2). Nevertheless, even when admixed after the reactor chamber, a significant conversion of n-butane is observed, which cannot just be attributed to oxidation by O_3. Instead further long-lived species, for example excited nitrogen species, are presumably enabling the oxidation process in the exhaust gas stream.

Data availability statement

The data that support the findings of this study are available upon reasonable request from the authors.

Acknowledgment

This study was funded by the German Research Foundation (DFG) with the Collaborative Research Centre CRC1316 'Transient atmospheric plasmas: from plasmas to liquids to solids' (projects A5 and A7).

Appendix. Full data sets of selected measurements

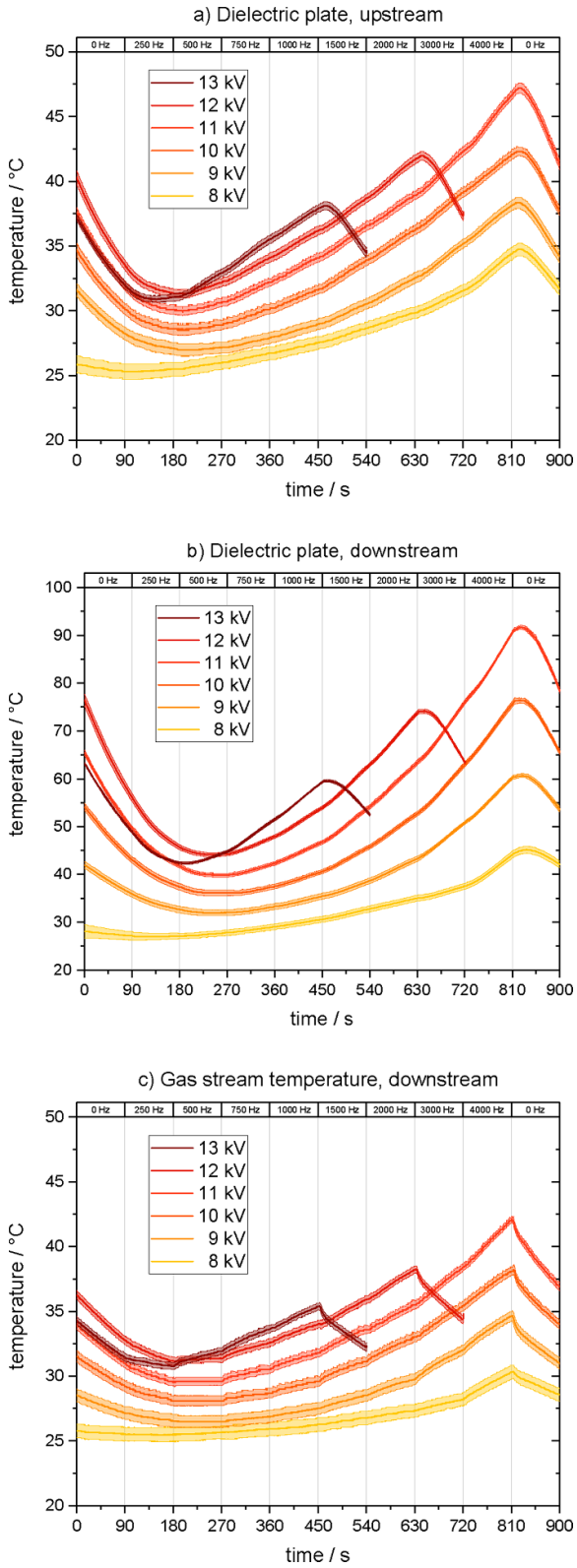

Figure A1. Temperatures measured on (a) the upstream end of the dielectric plate, (b) the downstream end of the dielectric plate, and (c) for the gas stream directly at the reactor outlet.

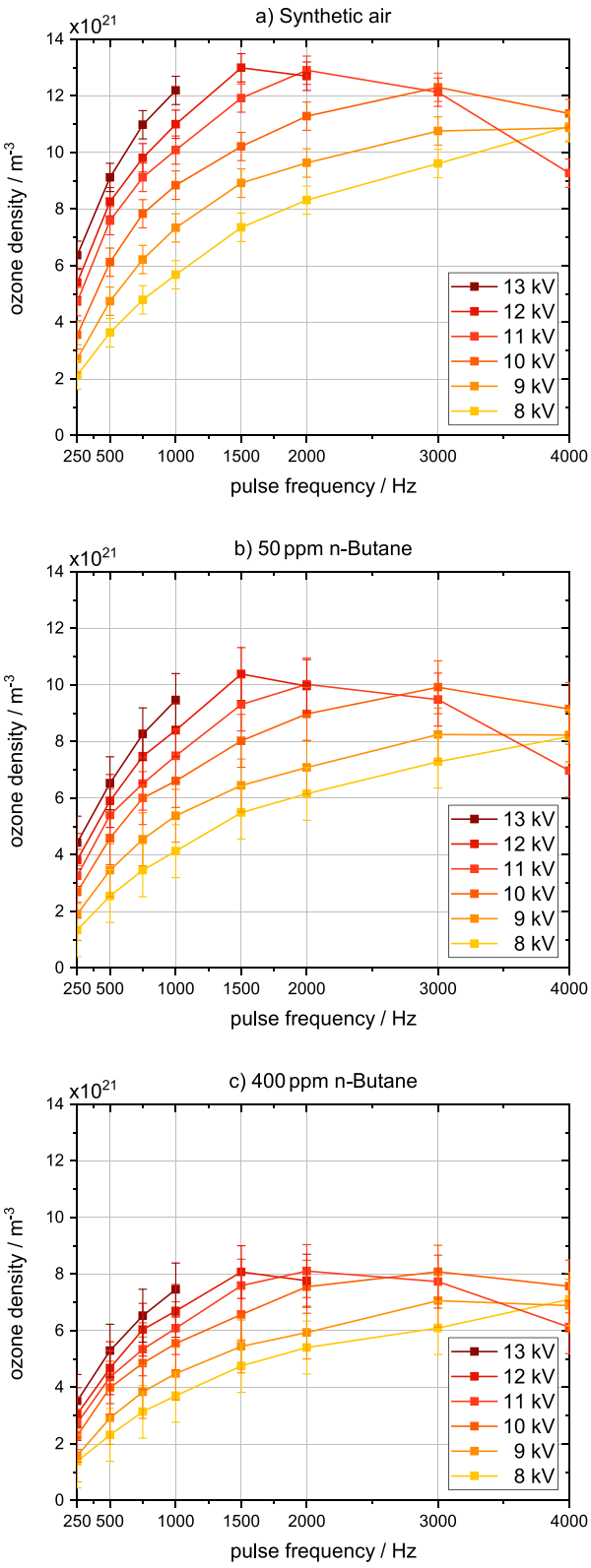

Figure A2. Densities of O_3 measured across the center of the discharge for (a) 0 ppm, (b) 50 ppm, and (c) 400 ppm of n-butane.

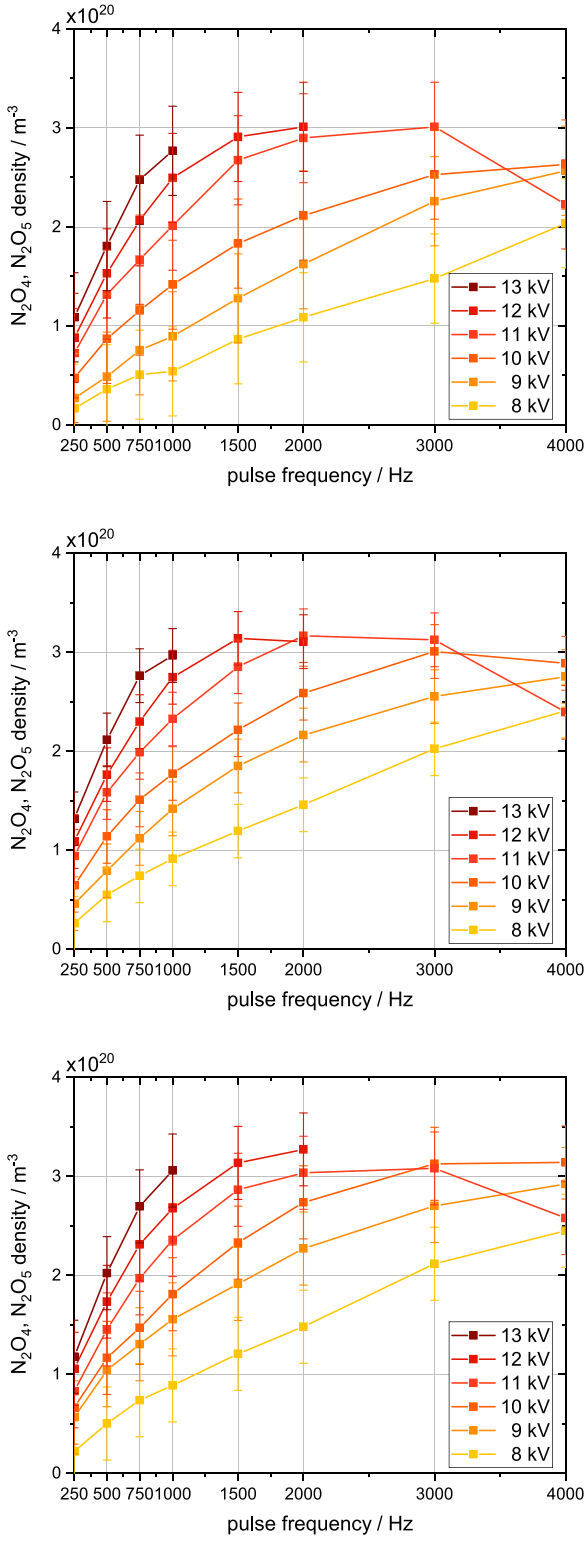

Figure A3. Densities of N_2O_4 measured across the center of the discharge for (a) 0 ppm, (b) 50 ppm, and (c) 400 ppm of n-butane.

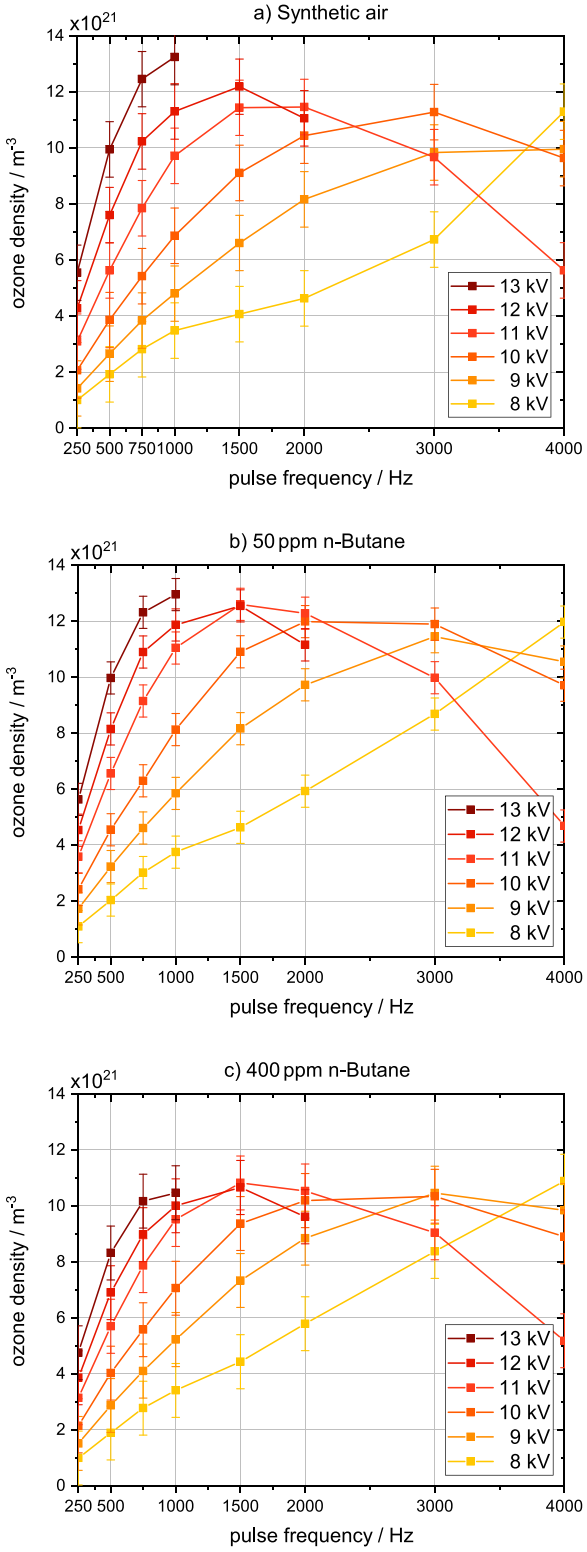

Figure A4. Densities of O_3 measured in the exhaust for (a) 0 ppm, (b) 50 ppm, and (c) 400 ppm of n-butane admixed before the plasma chamber.

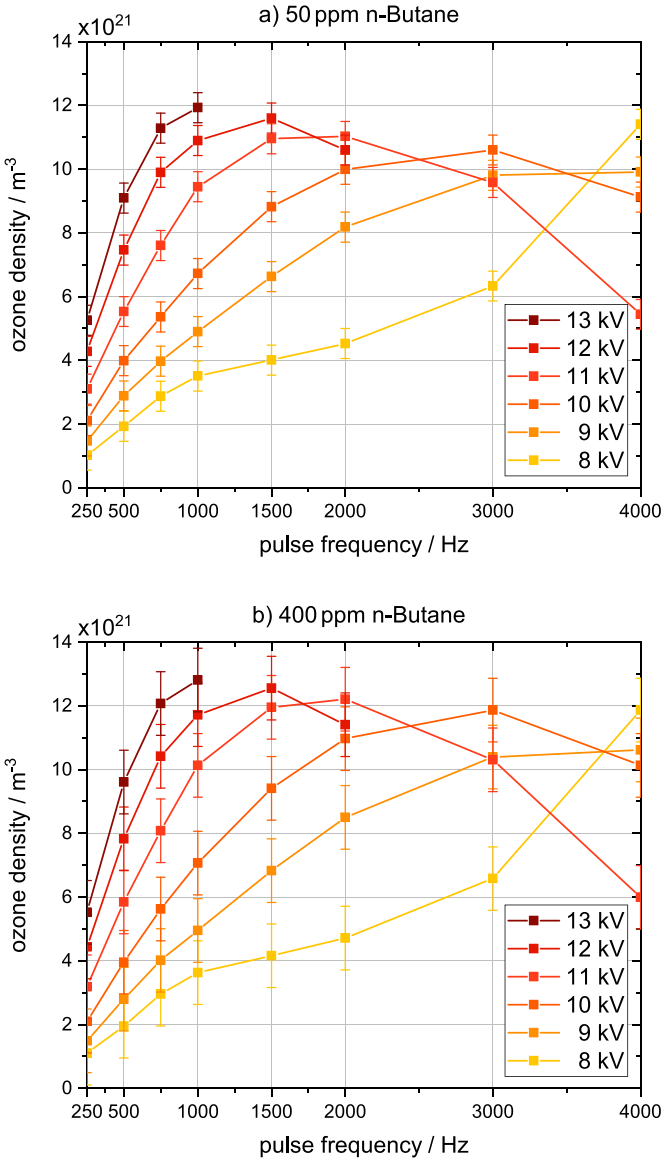

Figure A5. Densities of O_3 measured in the exhaust for (a) 50 ppm and (b) 400 ppm of n-butane admixed behind the plasma chamber.

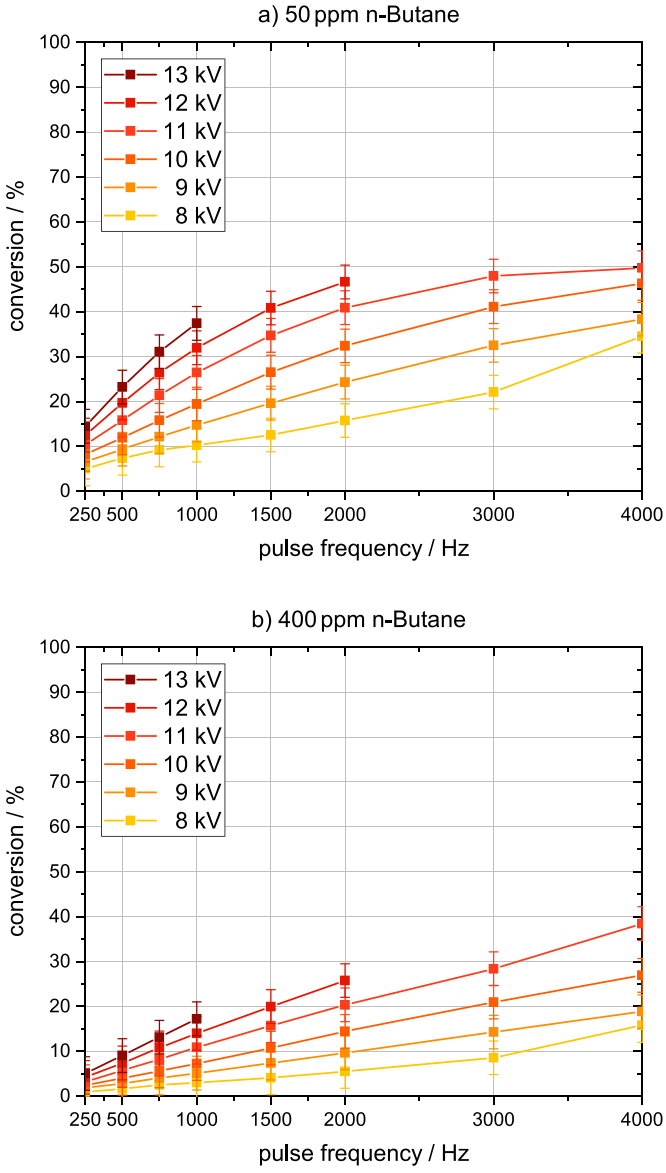

Figure A6. Relative conversion of n-butane when admixed before the reactor chamber for concentrations of (a) 50 ppm and (b) 400 ppm.

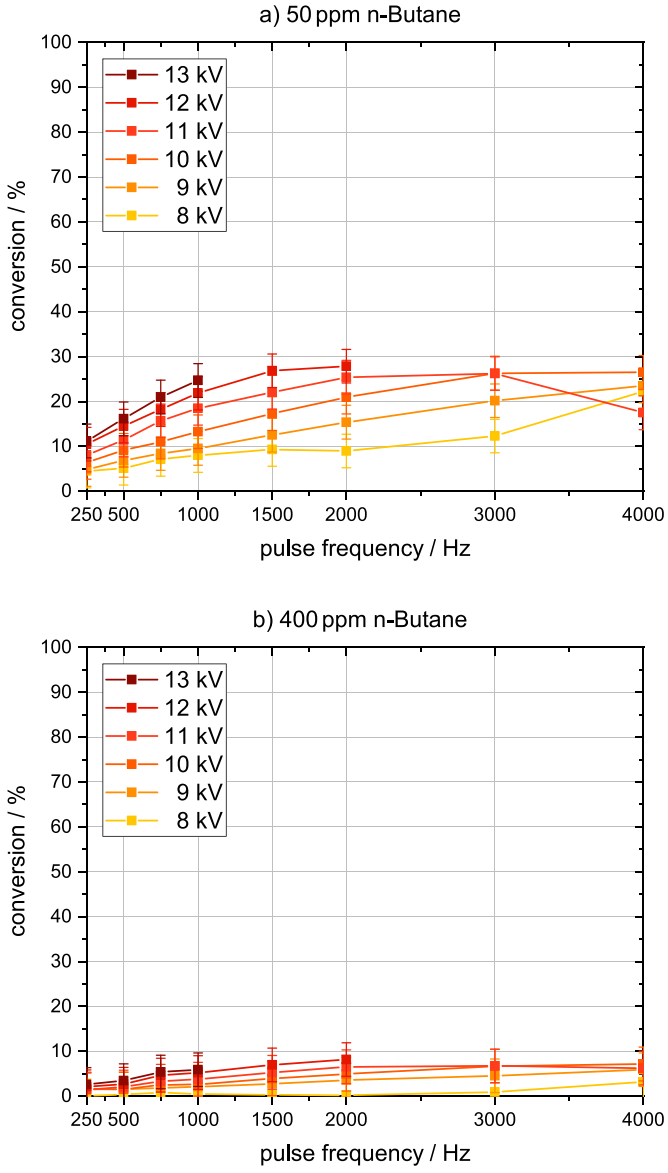

Figure A7. Relative conversion of n-butane when admixed after the reactor chamber for concentrations of (a) 50 ppm and (b) 400 ppm.

ORCID iDs

Lars Schücke https://orcid.org/0000-0002-7991-853X
Andrew R Gibson https://orcid.org/0000-0002-1082-4359
Martin Muhler https://orcid.org/0000-0001-5343-6922

References

[1] Weschler C J and Carslaw N 2018 Indoor chemistry *Environ. Sci. Technol.* **52** 2419–28
[2] Sakai K, Norbäck D, Yahong Mi, Shibata E, Kamijima M, Yamada T and Takeuchi Y 2004 A comparison of indoor air pollutants in Japan and Sweden: formaldehyde, nitrogen dioxide and chlorinated volatile organic compounds *Environ. Res.* **94** 75–85
[3] Liu Z and Little J C 2012 Materials responsible for formaldehyde and volatile organic compound (VOC) emissions *Toxicity of Building Materials, (Woodhead Publishing Series in Civil and Structural Engineering)*, ed F Pacheco-Torgal, S Jalali and A Fucic (Sawston: Woodhead Publishing) pp 76–121
[4] Guo H, Kwok N H, Cheng H R, Lee S C, Hung W T and Li Y S 2009 Formaldehyde and volatile organic compounds in Hong Kong homes: concentrations and impact factors *Indoor Air* **19** 206–17
[5] Norbäck D, Björnsson E, Janson C, Widström J and Boman G 1995 Asthmatic symptoms and volatile organic compounds, formaldehyde and carbon dioxide in dwellings *Occup. Environ. Med.* **52** 388–95
[6] Wiesländer G, Norbäck D, Björnsson E, Janson C and Boman G 1993 Asthma and the indoor environment: the significance of emission of formaldehyde and volatile organic compounds from newly painted indoor surfaces *Int. Arch. Occup. Environ. Health* **69** 1432
[7] Kim B R 2011 VOC emissions from automotive painting and their control: a review *Environ. Eng. Res.* **16**
[8] Choi B S and Yi J 2000 Simulation and optimization on the regenerative thermal oxidation of volatile organic compounds *Chem. Eng. J.* **76** 103–14
[9] Offerhaus B 2018 Characterisation of a novel twin surface dielectric barrier discharge designed for the purification of gas streams *Doctoral Thesis* Ruhr-Universität Bochum, Universitätsbibliothek
[10] Van Durme J, Dewulf J, Leys C and Van Langenhove H 2008 Combining non-thermal plasma with heterogeneous catalysis in waste gas treatment: a review *Appl. Catal. B: Environ.* **78** 324–33
[11] Vandenbroucke A M, Morent R, De Geyter N and Leys C 2011 Non-thermal plasmas for non-catalytic and catalytic VOC abatement *J. Hazardous Mater.* **195** 30–54
[12] Ju Li, Cunhua M, Zhu S, Feng Y and Dai B 2019 A review of recent advances of dielectric barrier discharge plasma in catalysis *Nanomaterials* **9** 1428
[13] Brandenburg R 2017 Dielectric barrier discharges: progress on plasma sources and on the understanding of regimes and single filaments *Plasma Sources Sci. Technol.* **26** 053001
[14] Kogelschatz U, Eliasson B and Egli W 1997 Dielectric-barrier discharges. Principle and applications *J. Phys. IV France* **07** 47–66
[15] Pietsch G J 2001 Peculiarities of dielectric barrier discharges *Contrib. Plasma Phys.* **41** 620–8
[16] Xin T, Whitehead J C and Nozaki T 2019 *Plasma Catalysis* (Berlin: Springer)
[17] Kogelheide F, Offerhaus B, Bibinov N, Krajinski P, Schücke L, Schulze J, Stapelmann K and Awakowicz P 2019 Characterisation of volume and surface dielectric barrier discharges in N_2–O_2 mixtures using optical emission spectroscopy *Plasma Process. Polym.* **17** 1900126
[18] Brandenburg R, Basner R and Weltmann K-D 2010 Nicht-thermische Plasmen zum Emissionsschutz *Vak. Forsch. Prax.* **22** 6–12
[19] Schmidt M, Schiorlin M and Brandenburg R 2014 Studies on the electrical behaviour and removal of toluene with a dielectric barrier discharge *Open Chem.* **13** 477–83
[20] Simoncelli E, Schulpen J, Barletta F, Laurita R, Colombo V, Nikiforov A and Gherardi M 2019 UV–VIS optical spectroscopy investigation on the kinetics of long-lived RONS produced by a surface DBD plasma source *Plasma Sources Sci. Technol.* **28** 095015
[21] Al-Abduly A and Christensen P 2015 An *in situ* and downstream study of non-thermal plasma chemistry in an air fed dielectric barrier discharge (DBD) *Plasma Sources Sci. Technol.* **24** 065006
[22] Moiseev T, Misra N N, Patil S, Cullen P J, Bourke P, Keener K M and Mosnier J P 2014 Post-discharge gas

composition of a large-gap DBD in humid air by UV–vis absorption spectroscopy *Plasma Sources Sci. Technol.* **23** 065033
[23] Wijaikhum A *et al* 2017 Absolute ozone densities in a radio-frequency driven atmospheric pressure plasma using two-beam UV-LED absorption spectroscopy and numerical simulations *Plasma Sources Sci. Technol.* **26** 115004
[24] Brisset A, Gibson A R, Schröter S, Niemi K, Booth J-P, Gans T, O'Connell D and Wagenaars E 2021 Chemical kinetics and density measurements of OH in an atmospheric pressure He + O_2 + H_2O radiofrequency plasma *J. Phys. D: Appl. Phys.* **54** 285201
[25] Schröter S *et al* 2018 Chemical kinetics in an atmospheric pressure helium plasma containing humidity *Phys. Chem. Chem. Phys.* **20** 24263–86
[26] Reuter S, Sousa J S, Stancu G D and van Helden J-P H 2015 Review on VUV to MIR absorption spectroscopy of atmospheric pressure plasma jets *Plasma Sources Sci. Technol.* **24** 054001
[27] Schücke L, Gembus J-L, Peters N, Kogelheide F, Nguyen-Smith R T, Gibson A R, Schulze J, Muhler M and Awakowicz P 2020 Conversion of volatile organic compounds in a twin surface dielectric barrier discharge *Plasma Sources Sci. Technol.* **29** 114003
[28] Peters N, Schücke L, Ollegott K, Oberste-Beulmann C, Awakowicz P and Muhler M 2021 Catalyst-enhanced plasma oxidation of n-butane over α-MnO_2 in a temperature-controlled twin surface dielectric barrier discharge reactor *Plasma Process. Polym.* **18** 2000127
[29] Keller-Rudek H, Moortgat G K, Sander R and Sörensen R 2013 The MPI-Mainz UV/VIS spectral atlas of gaseous molecules of atmospheric interest *Earth Syst. Sci. Data* **1** 365–73
[30] Shimizu T, Sakiyama Y, Graves D B, Zimmermann J L and Morfill G E 2012 The dynamics of ozone generation and mode transition in air surface micro-discharge plasma at atmospheric pressure *New J. Phys.* **14** 103028
[31] Park S, Choe W and Jo C 2018 Interplay among ozone and nitrogen oxides in air plasmas: rapid change in plasma chemistry *Chem. Eng. J.* **352** 1014–21
[32] Barnes J and Mauersberger K 1987 Temperature dependence of the ozone absorption cross section at the 253.7 nm mercury line *J. Geophys. Res.: Atmos.* **92** 14861–4
[33] Federal Ministry of Justice and Consumer Protections 2021 Standard Reference Database 17, Version 7.0 (Web Version), Release 1.6.8, Data Version 2015.09 (available at: https://kinetics.nist.gov/kinetics/Detail?id=1985POP/EGO273:1) (Online; accessed 14 July 2021)
[34] Chai J and Franklin Goldsmith C 2017 Rate coefficients for fuel+NO_2: predictive kinetics for HONO and HNO_2 formation *Proc. of the Combustion Institute* vol 36 pp 617–26
[35] Badra J, Nasir E F and Farooq A 2014 Site-specific rate constant measurements for primary and secondary H- and D-abstraction by OH radicals: propane and n-butane *J. Phys. Chem.* A **118** 4652–60
[36] Miyoshi A, Ohmori K, Tsuchiya K and Matsui H 1993 Reaction rates of atomic oxygen with straight chain alkanes and fluoromethanes at high temperatures *Chem. Phys. Lett.* **204** 241–7
[37] Datta R K and Rao K N 1979 Kinetics of reactions of singlet molecular oxygen($^1{}_g$) with organic compounds *J. Phys. Chem. Ref. Data* **18** 102–5 (http://nopr.niscair.res.in/handle/123456789/51307)
[38] Schubert C C, Schubert S J and Pease R N 1956 The oxidation of lower paraffin hydrocarbons. I. Room temperature reaction of methane, propane, n-butane and isobutane with ozonized oxygen *J. Am. Chem. Soc.* **78** 2044–8
[39] Atkinson R, Baulch D L, Cox R A, Crowley J N, Hampson R F, Hynes R G, Jenkin M E, Rossi M J and Troe J 2004 Evaluated kinetic and photochemical data for atmospheric chemistry: volume I - gas phase reactions of O_x, HO_x, NO_x and SO_x species *Atmos. Chem. Phys.* **4** 1461–738
[40] Warnatz J 1984 *Rate Coefficients in the C/H/O System* (New York: Springer) pp 197–360
[41] Herron J T 1999 Evaluated chemical kinetics data for reactions of N(^{2}D), N(^{2}P) and $N_2(A^3\Sigma_u^+)$ in the gas phase *J. Phys. Chem. Ref. Data* **28** 1453–83
[42] Fell B, Rivas I V and McFadden D L 1981 Kinetic study of electronically metastable nitrogen atoms, N(2^2D_J), by electron spin resonance absorption *J. Phys. Chem.* **85** 224–8
[43] Umemoto H, Sugiyama K, Tsunashima S and Sato S 1985 Collisional deactivation of N(2^2P) atoms by simple molecules *Bull. Chem. Soc. Japan* **58** 3076–81
[44] Callear A B and Wood P M 1971 A system of HNO in the far ultra-violet and measurement of its oscillator strength *Trans. Faraday Soc.* **67** 3399–406
[45] Federal Ministry of Justice and Consumer Protections 2021 Standard Reference Database 17, Version 7.0 (Web Version), Release 1.6.8, Data Version 2015.09 (available at: https://kinetics.nist.gov/kinetics/rpSearch?cas=106978) (Online; accessed 14 July 2021)
[46] Ollegott K, Wirth P, Oberste-Beulmann C, Awakowicz P and Muhler M 2020 Fundamental properties and applications of dielectric barrier discharges in plasma-catalytic processes at atmospheric pressure *Chem. Ing. Tech.* **92** 1542–58